sustainability

MDPI

Article

Study on Crack Classification Criterion and Failure Evaluation Index of Red Sandstone Based on Acoustic Emission Parameter Analysis

Jiashen Li [1,2], Shuailong Lian [1,2], Yansen Huang [1,2] and Chaolin Wang [1,2,*]

[1] College of Civil Engineering, Guizhou University, Guiyang 550025, China; gs.lijs19@gzu.edu.cn (J.L.); gs.sllian19@gzu.edu.cn (S.L.); yshuang_gu@126.com (Y.H.)
[2] Guizhou Provincial Key Laboratory of Rock and Soil Mechanics and Engineering Safety, Guiyang 550025, China
* Correspondence: clwang3@gzu.edu.cn

Abstract: The acoustic emission (AE) characteristics of rock during loading can reflect the law of crack propagation and evolution in the rock. In order to study the fracture mode in the process of rock fracture, the AE characteristics and crack types of red sandstone during fracture were investigated by conducting Brazilian indirect tensile tests (BITT), direct shear tests (DST), and uniaxial compression tests (UCT). The evolution law of AE event rate, RA and AF values, and the distribution law of RA–AF data of red sandstone samples in three test types were analyzed. Based on the kernel density estimation (KDE) function and the coupling AE parameters (RA–AF values) in DST and BITT, the relatively objective dividing line for classifying tensile and shear cracks was discussed, and the dividing line was applied to the analysis of fracture source evolution and the failure precursor of red sandstone. The results show that the dividing line for classifying tensile and shear cracks of red sandstone is AF = 93RA + 75. Under uniaxial compression loading, the fracture source of red sandstone is primarily shear source in the initial phase of loading and tensile source in the critical failure phase, and the number is far greater than shear source. K = AF/(93RA + 75) can be defined as the AE parameter index, and its coefficient of variation CV (k) can be used as the failure judgment index of red sandstone. When CV (k) < 1, it can be considered that red sandstone enters the instability failure phase.

Keywords: acoustic emission; sensor; parameter analysis; RA and AF; crack classification criterion

Citation: Li, J.; Lian, S.; Huang, Y.; Wang, C. Study on Crack Classification Criterion and Failure Evaluation Index of Red Sandstone Based on Acoustic Emission Parameter Analysis. *Sustainability* **2022**, *14*, 5143. https://doi.org/10.3390/su14095143

Academic Editors: Longjun Dong, Yanlin Zhao and Wenxue Chen

Received: 18 March 2022
Accepted: 21 April 2022
Published: 24 April 2022

1. Introduction

Brittle rock is a complex geological medium, in which microcracks will occur under loading, and with the propagation and connection of microcracks on different scales, the rock will be damaged [1–4]. Furthermore, in a variety of rock engineering applications, red sandstone, as sedimentary rock, has been used widely [5–7]. Hence, studying the failure characteristics of red sandstone is of great significance for stability monitoring and disaster early warning in engineering projects [8–10]. When the rock is damaged, it will produce an acoustic emission (AE), which is essentially the elastic wave released in the process of crack generation and propagation [11–14]. In fact, the AE characteristics of rock during loading can reflect the law of crack propagation and evolution in the rock [15–19].

AE parameters can be divided into time domain parameters and frequency domain parameters, which are all extracted from the AE time domain waveform [20–23]. The time domain parameters of AE signals most widely used to reveal the rock failure mechanism are: rise time, duration, AE count, maximum amplitude, energy, and average frequency (AF) [24–28], as shown in Figure 1a. The frequency domain parameters of AE signal most widely used are peak frequency, frequency centroid, and partial power; peak frequency

is the point corresponding to the maximum amplitude in the frequency spectrum, the frequency centroid, representing the center of mass of the AE signal, is calculated from a sum of magnitude time frequencies divided by a sum of magnitude, and partial power is calculated from the sum of the frequency spectrum within a specified range divided by the total power of all frequencies [29,30]. In addition, in AE field monitoring, in order to improve the accuracy of monitoring and disaster early warning, the location of the fracture source has gradually become an important development direction [31].

As regards the cracking type of brittle materials, AE signals from tensile cracking and shear cracking have different characteristics. The source type can be classified by tracking the characteristics of an AE signal to improve the understanding of the rock cracking mode. The time domain parameters commonly used to classified cracking type are the rise angle (RA) and average frequency (AF) [32–34]. The RA value is defined as the ratio of rise time to amplitude, in ms/V; the AF value, the number of threshold crossings (i.e., counts) over the duration of the AE signal, is the ratio of counts to duration, in kHz [35–38]. Generally, tensile fracture corresponds to an AE signal with low RA value and high AF value, while shear fracture corresponds to an AE signal with high RA value and low AF value [13,39], as shown in Figure 1b. Based on the above conclusions, the damage mechanism and failure mode classification of brittle materials can be analyzed by the RA and AF values of the AE signals in previous studies. Based on the analysis of RA and AF values, some scholars have investigated the damage mechanism and failure mode of different materials, such as hollow slab specimens of calcite and marble, ice structures, rubber powder concrete, and other rock types, in several basic lab tests [40–43]. Meanwhile, many scholars have investigated the effects of strain rate, brittleness, bedding, microwave radiation, and crack on rock failure mode by analyzing RA and AF values [44–50]. In addition, Muñoz-Ibáñez et al. compared the advantages and disadvantages of semicircular bending (SCB) and pseudo compact stretching (PCT) by analyzing the RA and AF values [51]. In addition, frequency domain parameters are often used to classified rock fracture types. For example, in order to effectively classify source types, based on peak frequency or partial power, Zhang et al. proposed a new source classification criterion [30]. Li et al. studied the dominant frequency characteristics of the AE signal of marble based on direct tensile tests, and showed that the low-frequency waveform represents tensile cracking and the high-frequency waveform represents shear cracking [52].

However, when focusing on the cracking type classification of brittle materials based on RA and AF values, there is no clear standard for the boundary between RA and AF values. Niu et al. determined that the proportional relationship between RA and AF values is 2:1 in their evaluation for the classification of fracture modes of flawed red sandstone under uniaxial compression [53]. Wang et al. proposed that the proportional relationship between RA and AF values is 1:3.75 when investigating the influence of multistage cyclic loading on the classification of marble fracture mode [54,55]. Yao et al. proposed that the proportional relationship between RA and AF values is 1:2 when investigating the effect of moisture on the failure mode in coal [56]. Fan et al. proposed that the proportional relationship between RA and AF values is 50:1 when investigating the fracture behavior of fully graded concrete under three-point bending loading at different loading rates [57]. Moreover, the intercept was introduced when some scholars investigated crack classification criteria based on RA and AF values. Das et al. proposed that the optimal dividing line for classifying the fracture type of strain hardening cementitious composite (SHCC) specimens is $AF = 26.9841RA - 268.6918$ [58]. Du et al. proposed that the optimal dividing line for classifying the fracture type of marble is $AF = 400RA + 50$, when studying the AE characteristics of marble [26]. In addition, when analyzing the precursory characteristics of rock instability, Dong et al. proposed that the ratio of RA to AF is 1:200, and found that the anisotropic characteristics of AE event rate can effectively reveal the failure precursors of rock mass, and determine the direction of principal stress [59].

It can be seen from the above analysis that the rock cracking type classification based on RA and AF values is mainly derived from the empirical relationship between RA and AF values, which is uncertain and empirical; that is, the boundary between shear cracking and tensile cracking has not been determined. Therefore, it is particularly important to determine the relatively objective boundary between tensile and shear cracking. Nowadays, many scholars use the cluster analysis method to determine the optimal dividing line [58,60,61], and many scholars use the kernel density estimation (KDE) function, a non-parametric density estimation method [53–55]. In addition, some scholars investigated the RA–AF characteristics of rock under direct tensile failure modes by conducting a direct tensile test, to determine the optimal dividing line [25,52]. However, most of the above research methods focused on a single loading condition, and the single application of a mathematical analysis method could not fully reflect the fracture type of rock. In addition, the reliability of the dividing line verified in the above research is still low. In this paper, the AE characteristics of red sandstone during the fracture process were investigated by conducting BITT, DST, and UCT. At the same time, based on the KDE function, the AE data collected in BITT and DST are coupled to discuss the dividing line for classifying red sandstone cracking type, and the reliability of the dividing line is verified. In addition, the corresponding precursory characteristic parameters of rock failure are proposed based on the determined dividing line.

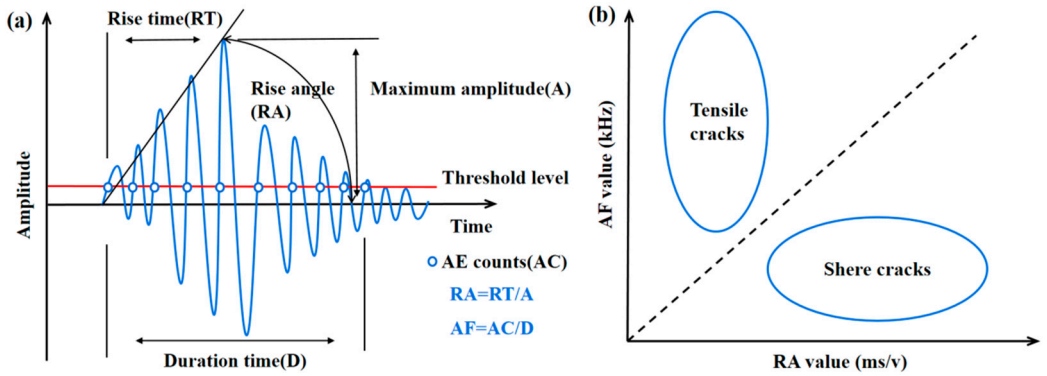

Figure 1. Typical AE waveform and micro fracture (crack) classification. (**a**) AE parameter in a hit; (**b**) crack classification based on RA/AF value.

2. Materials and Experimental Methods

2.1. Specimen Preparation

The origin of the light brown sandstone blocks used in the experimental testing is the northwestern Sichuan Basin, China. The P-wave and average density of sandstone blocks are measured as 3270 m/s and 2390 kg/m^3, respectively. All specimens used in the lab tests came from the same rock block and were cut in the same direction to avoid specimen dispersion. In this testing, nine specimens were prepared in three sizes. The side of the cube specimen used in DST was 100 mm, the size of disc specimen used in BITT was $\Phi 50 \times H25$ mm, and the size of the cylindrical specimens used in UCT was $\Phi 50 \times H100$ mm. The geometry and dimensions of the specimens in the three test types are shown in Figure 2. The accuracy of each specimen is within the range specified by ISRM.

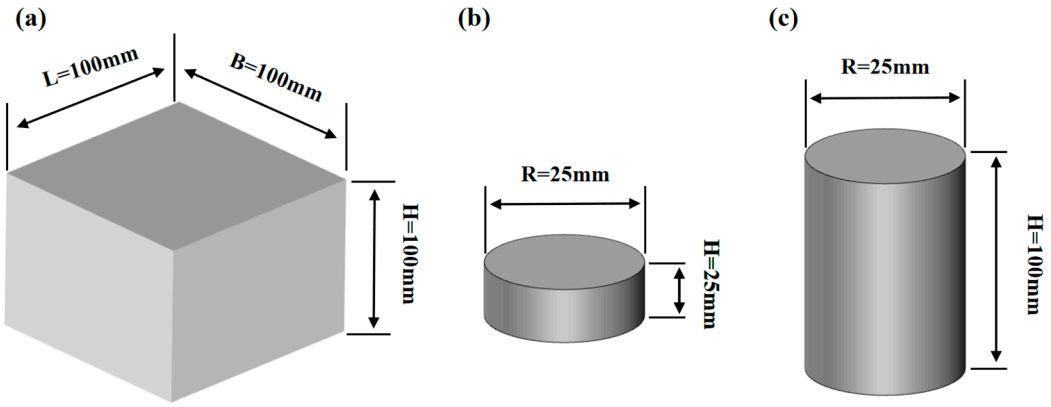

Figure 2. The geometry and dimensions of the specimens in the three types. (**a**) DST; (**b**) BITT; (**c**) UCT.

2.2. Experimental Equipment and Setup

(1) Loading equipment

The designed DST was conducted on the WDAJ-600 rock shear testing machine. The maximum loading value of the WDAJ-600 test machine in the vertical and horizontal directions is 600 kN, and its loading accuracy is ±0.5%. In addition, the designed BITT and UCT were conducted in the DSZ-1000 stress–strain controlled testing system. The maximum loading value of the DSZ-1000 test machine is 1000 kN, and its loading accuracy is also ±0.5%.

In this study, in order to ensure that the shape of the specimen will not be damaged by the indenter of the testing machine when specimen failure occurs, the displacement control mode was selected as the loading mode. In DST and UCT, the loading rate was 0.1 mm/min. In BITT, since the length of the specimen along the loading direction was half of those in the DST and UCT, the displacement rate was 0.05 mm/min. The normal stress of DST was 1 MPa. Before the formal loading, the force of 0.5 kN was applied to the specimens in DST and BITT, and the force of 1 kN was applied to the specimens in UCT, which ensured that the specimens were in full contact with the loading device, so as to further eliminate the noise generated during the contact between the specimens and the loading device in the formal test.

(2) AE monitoring system

The PCI-2 AE monitoring system was used to collect the AE signals during the deformation and damage of the specimen, and its manufacturer was the American Acoustics Company. The preamplifier gain of the AE monitoring system was set to 40 dB, which was used to increase the anti-interference ability of weak signals. The threshold was also set to 40 dB; that is, AE signals whose amplitude exceeded 40 dB were recorded. The sampling length of the single waveform and sampling rate was set to 2 k and 5 MSPS, respectively. The sensor used was a PICO sensor with a resonant frequency of 150 kHz. The operating frequency range was set to 20–400 kHz.

When installing the sensor on the surface of the sample, firstly, a layer of coupling agent was applied on the sensor, to ensure that there was no gap between the sensor and the rock surface; secondly, four sensors coated with coupling agent were placed on the surface of the rock sample using black insulating tape. Black insulating tape has good elasticity, so it can stabilize the sensor and also protect it from being crushed. The above measures ensured that the collected acoustic emission signal was not distorted.

Before the formal loading, a "pencil lead breaking test" was conducted to check whether all channels were connected normally, so as to further ensure that the AE signals can be collected effectively. The pencil lead fracture is a practical pulse simulation source. Pencil lead fractures are used to simulate the acoustic emission signal generated by concrete deformation and fracture.

All testing systems used are shown in Figure 3. The types of tests, the distribution of AE sensors and damaged rock specimens are shown in Figure 4.

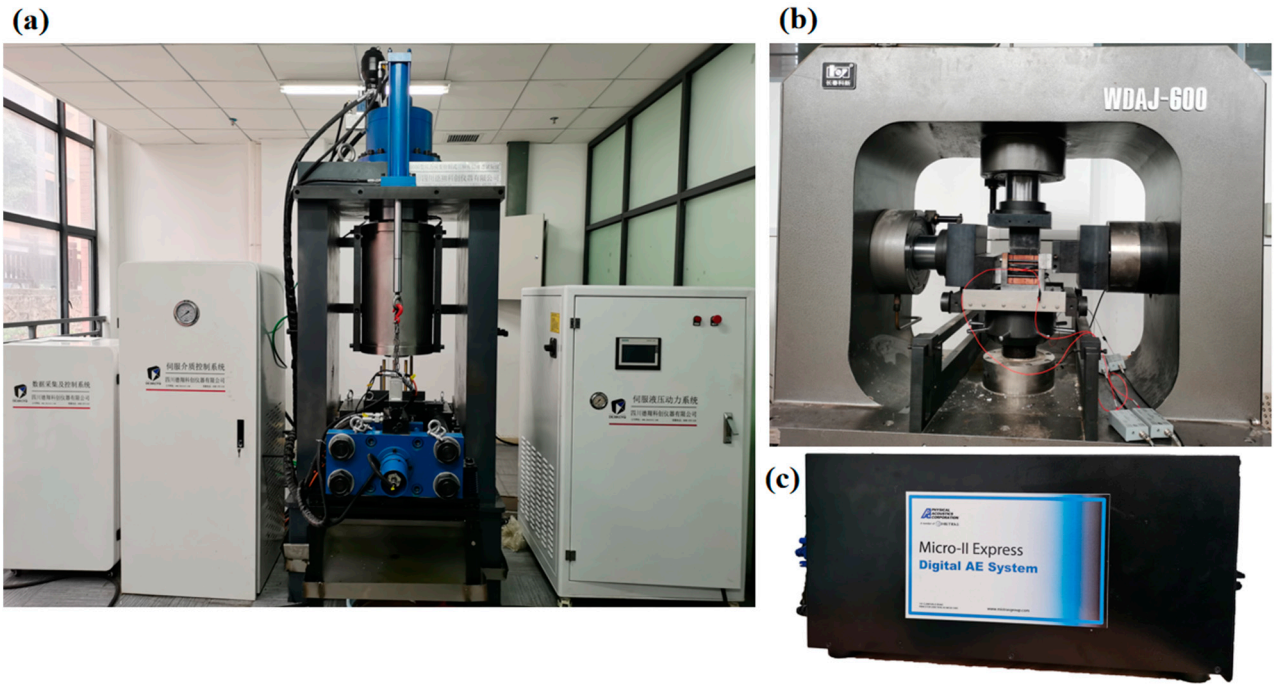

Figure 3. Testing systems used in this study: (**a**) DSZ-1000 stress–strain controlled testing system; (**b**) WDAJ-600 rock shear testing machine; (**c**) PCI-2 AE monitoring.

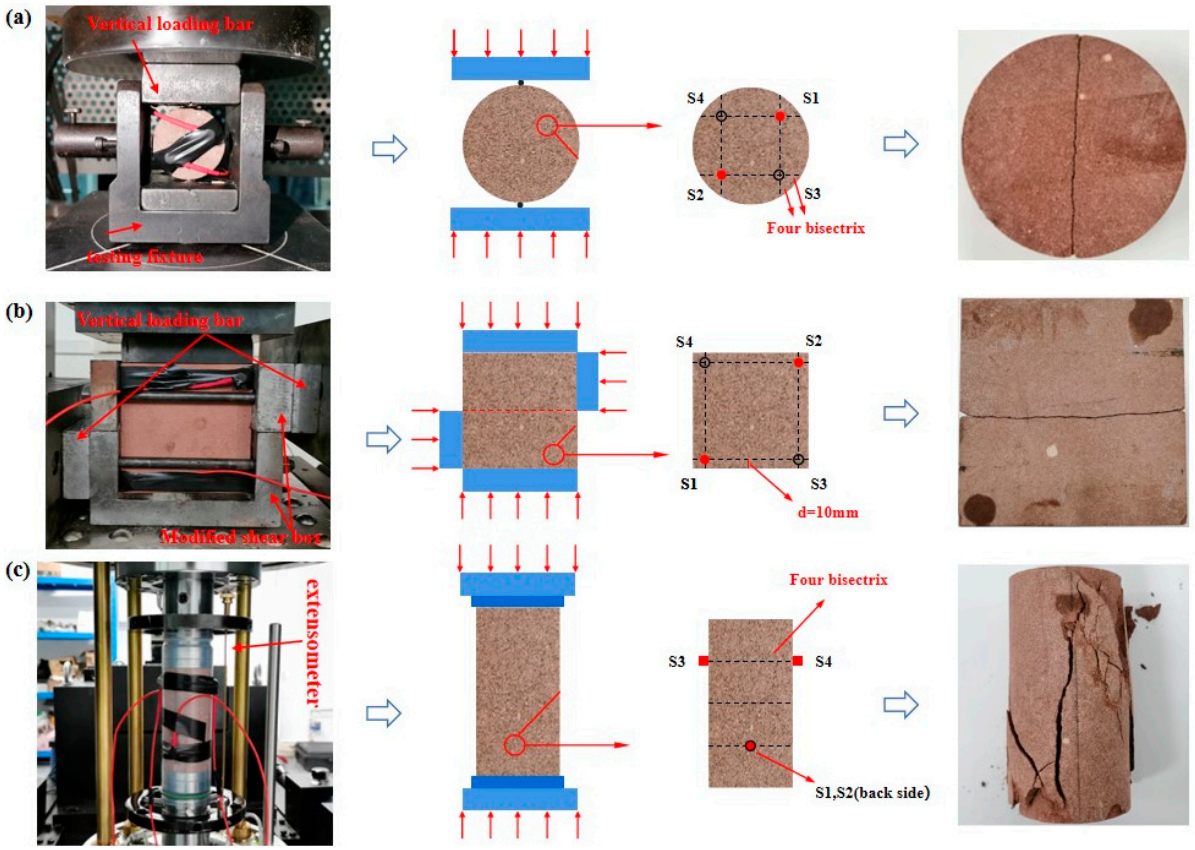

Figure 4. Types of test, the distribution of AE sensors and damaged rock specimens. (**a**) BITT; (**b**) DST; (**c**) UCT.

Three identical rock samples were set up in each test type to eliminate the effect of discreteness on the test results. The stress–displacement curve or stress–strain curve of the specimens in each of the three test types is shown in Figure 5. The strain data were collected by an extensometer, so the stress–strain curve could be drawn in UCT, while in DST and BITT, only stress displacement curves could be drawn. In addition, the number and strength of all specimens are shown in Table 1, in which σ_t, σ_s and σ_c denote the tensile strength (MPa), the shear strength (MPa), and the uniaxial compressive strength (MPa), respectively.

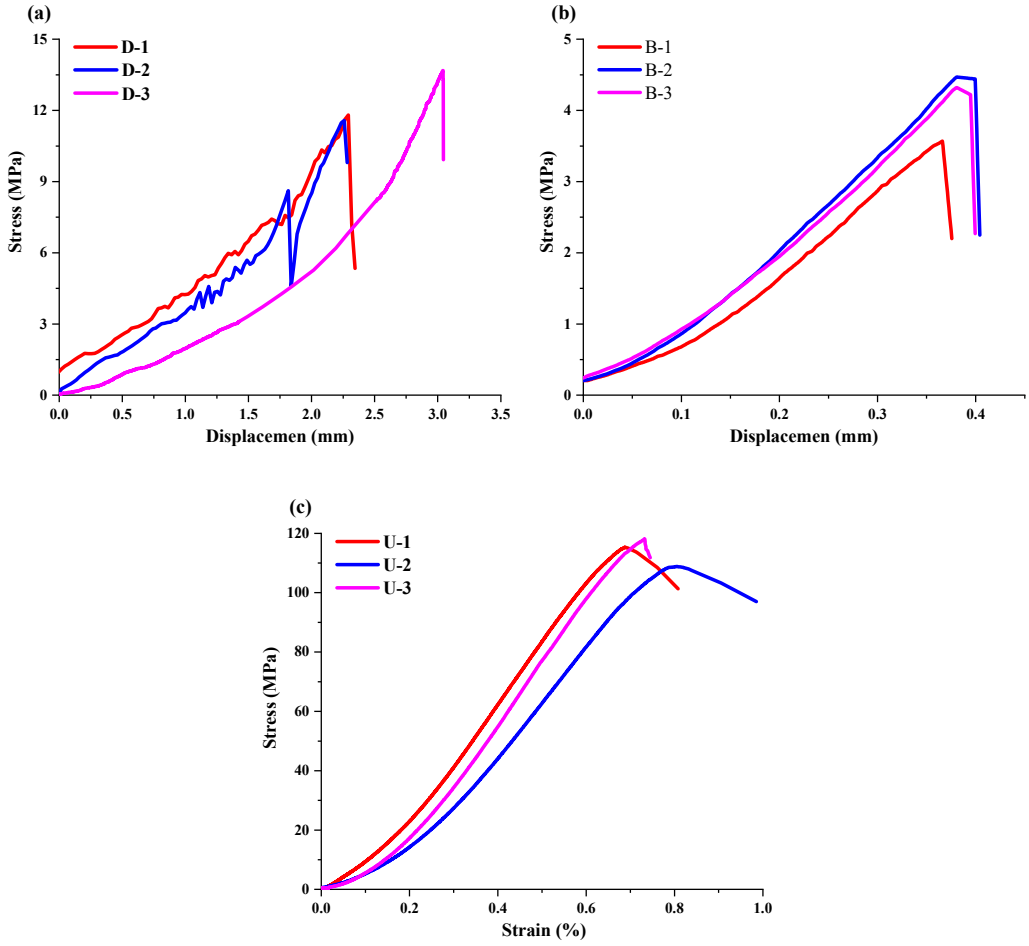

Figure 5. The stress–displacement curve or stress–strain curve of the specimen in three test types. (**a**) DST; (**b**) BITT; (**c**) UCT.

Table 1. Basic physical and mechanical parameters of red sandstone.

Number	Type of Test	Loading Rate (mm/min)	$\sigma_t/\sigma_s/\sigma_c$ (MPa)
B-1	BITT	0.05	7.06
B-2			8.50
B-3			8.80
D-1	DST	0.1	12.48
D-2			11.79
D-3			13.68
U-1	UCT	0.1	115.27
U-2			108.79
U-3			118.10

3. AE Data Processing Methods

The AE event rate is represented by event interval function F(τ), which can reveal the crack propagation of rock specimens, from microcracking to macrocracking. Based on the RA and AF values, the fracture mode of the red sandstone in the loading process was analyzed, and the classification method of the red sandstone fracture mode was determined. In addition, the KDE function was adopted to visualize the RA–AF data density maps. In this chapter, we focus on the three adopted AE data processing methods.

3.1. Inter-Event Time Function F(τ) Theory

The basic connotation of the inter-event time function F(τ) is the average occurrence frequency of N AE events that move continuously, and τ represents the time interval of N AE events [62]. The derivation process is as follows [16]:

$$\Delta t_i = t_i - t_{i-1}, i = 2, 3, \ldots \tag{1}$$

where t_i is the time of the i-th AE event, and t_{i-1} is the time of the previous AE event.

$$\tau_i = \frac{t_{\mathrm{N}+i-1} - t_{i-1}}{\mathrm{N}}, i = 2, 3, \ldots \tag{2}$$

$$\tau_1 = \frac{t_N - t_1}{\mathrm{N}} \tag{3}$$

$$\mathrm{F}(\tau_\mathrm{i}) = \tau_i^{-1}, i = 1, 2, \ldots \tag{4}$$

When calculating F(τ) in this paper, the N-value of all samples is taken as 50. Furthermore, it is worth noting that F(τ) for N − 1 acoustic emission events cannot be defined, but this does not affect the accuracy of the overall test results.

3.2. RA and AF Values Method

Since the unit of amplitude is dB, it is necessary to convert the unit dB into voltage unit V, and the conversion formula is shown in Formula (5) [37]. RA and AF values are calculated according to the basic parameters of the AE signal, and the calculation method is shown in Formulas (6) and (7) [32].

$$B(\mathrm{mV}) = 10^{\frac{A(dB)}{20} - 1} \tag{5}$$

$$RA\ value = \frac{Rise\ time}{Maximum\ amplitude} \tag{6}$$

$$AF\ value = \frac{Count}{Duration\ time} \tag{7}$$

3.3. Kernel Density Estimation (KDE) Method

The KDE method is widely used in data analysis. In this study, the KDE method was utilized to identify and visualize high-density regions of RA and AF values. The basic principles of the KDE approach are as follows [63].

The basic idea of the KDE method is that each point in the estimated data contributes an "atom" of probability density to the estimate, and $p(z)$ is used to represent the true density estimate of multivariate data. The formula is as follows:

$$\hat{p}(\underline{z}) = \frac{1}{nh}\sum_{i=1}^{n} K\left(\frac{\underline{z} - \underline{Z_i}}{h}\right) \tag{8}$$

where n is the total number of estimated samples, h is the smoothing parameter controlling the atomic width, and Z_i represents the i-th data point. $K(x)$ is a kernel function. In this paper, the multivariate Gaussian function is taken as the kernel function, and its formula is as follows:

$$K(\underline{x}) = \frac{1}{(2\pi)^{\frac{d}{2}}} exp\left(-\frac{1}{2}\|x\|^2\right) \quad (9)$$

where d denotes the dimension of data space.

The probability density function values for all sample points can be simply obtained by establishing an estimate $p(z)$.

The accuracy of the estimate is affected by the value of h and the size of the sample, so the value of h must be reasonably determined. Since the least squares cross-validation method has a large advantage in reducing the squared error between the density estimate and the actual density, this method has been selected to determine the value of h in this paper. The calculation formula of square error is as follows:

$$J[\hat{p}] = \int [p(\underline{x}) - \hat{p}(\underline{x})]^2 \, d\underline{x} \quad (10)$$

When the real density is Gaussian, the optimal smoothing parameters can be determined by the following formula:

$$h^* = Bn^{1/(d+4)} \quad (11)$$

where parameter B is related to parameter d, and its expression of multivariate distribution is shown as:

$$B = \begin{cases} 1 \; when \; d = 2 \\ (\frac{4}{d+2})^{\frac{1}{d+4}} \; otherwise \end{cases} \quad (12)$$

4. Experimental Results

The AE data of different samples have good consistency in the BITT, DST, and UCT. Therefore, the data of the specimen with the greatest strength were selected for analysis, such as B-3, D-3, and U-3. Simultaneously, the characteristic of the AE event rate in the whole process of the test was analyzed to reveal the AE activity in the process of sample damage and fracture by the time function f between events F(τ). In this section, the evolution law of the AE event rate, the RA and AF values, and the distribution law of RA–AF data in three test types were analyzed.

4.1. AE Event Rate Monitoring

Figure 6 shows the evolution characteristics of the AE event rate and stress with time for the red sandstone samples in the three types of tests. In Figure 6, the vertical coordinate includes stress (black), the number of accumulative AE events (blue), and its corresponding AE event rate (F(τ), pink); the horizontal coordinate is the time of each test type. The whole process of rock damage and fracture is divided into phase-1 and phase-2, according to the evolution law of the AE event rate with time. In phase-1, the AE event rate showed a relatively steady state, and the cumulative AE events grew slowly, which indicates that the crack initiation and expansion activities in rock are moderate. Therefore, phase-1 is called the gentle growth period of AE events (microcrack generation phase). Further, phase-2 is called the sharp growth period of AE events (macrocrack generation phase). In phase-2, the AE event rate increases gradually with a state of high and low fluctuation, and the cumulative AE events increase sharply, which indicates that the crack propagation activity in the critical failure stage in the rock is intense, and macroscopic cracks gradually form, showing a failure trend. The critical time point between adjacent phases is considered to be T_t, and F_t is the corresponding load at T_t. F_t is expressed as $F_t = kF_p$, where F_p is the peak load and k is the ratio of F_t to F_p. In addition, the proportion of AE events in phase-1 and phase-2 to the total number of events in each test type is shown in Figure 7.

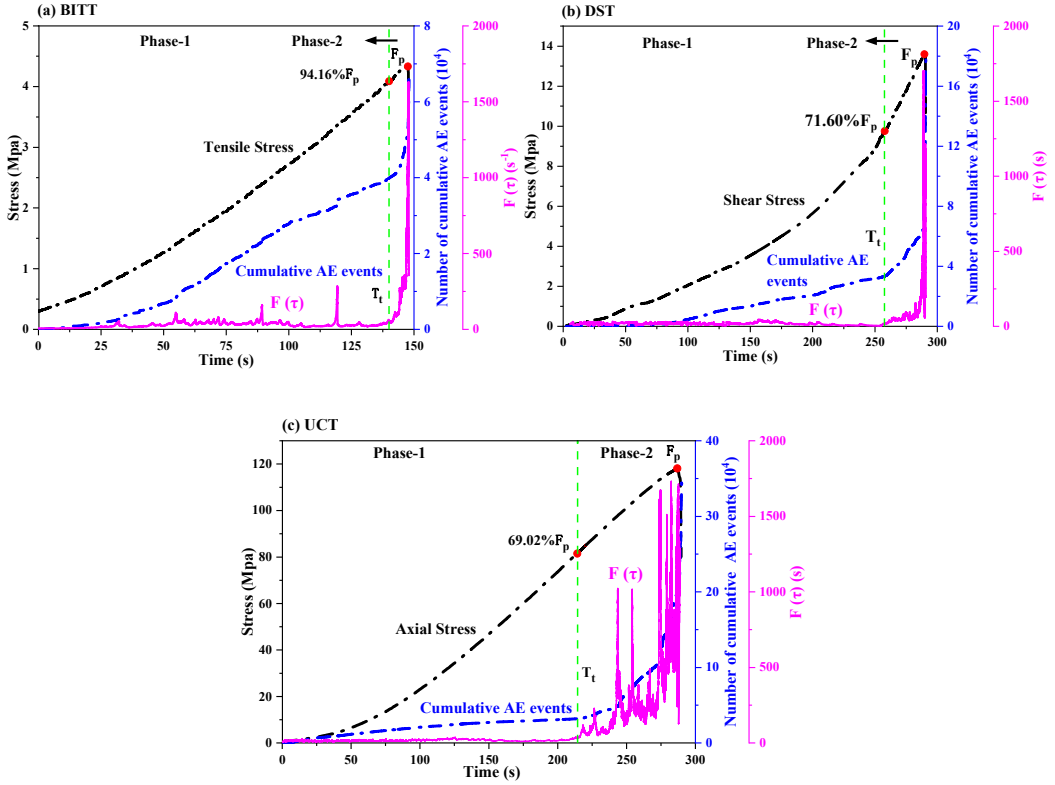

Figure 6. Variations of stress, cumulative AE events and corresponding AE event rate with time. (**a**) BITT; (**b**) DST; (**c**) UCT.

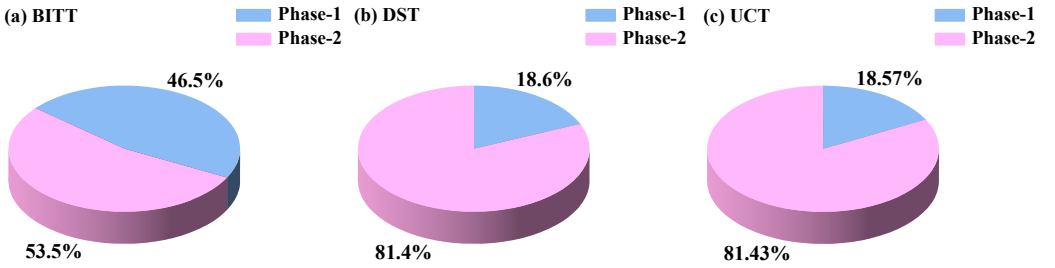

Figure 7. The proportion of AE events in phase-1 and phase-2 to the total number of events. (**a**) BITT; (**b**) DST; (**c**) UCT.

In BITT, the number of AE events in phase-1 and phase-2 accounts for 46.48% and 53.52% of the total events, respectively. In DST, the number of AE events in phase-1 and phase-2 accounts for 18.57% and 81.43% of the total events, respectively. In UCT, the number of AE events in phase-1 and phase-2 accounts for 17.33% and 82.67% of the total events, respectively. On the whole, nearly half of the AE events in BITT occurred before loading F_t, indicating that the rock has been damaged to a certain extent in the microcrack generation phase. However, in DST and UCT, the number of AE events is less before loading F_t, which indicates that the rock damage mainly occurs in the macrocrack generation phase. In addition, the F_t in BITT, DST, and UCT are 94.16% F_p, 69.02% F_p and 71.81% F_p, respectively. It can be seen that the macrocrack generation phase in BITT is significantly shorter than that in DST and UCT. The above results are due to the different fracture modes of rocks under different loading conditions. In BITT, tensile fracture mainly occurs; in DST, shear fracture mainly occurs; and in UCT, tensile and shear fracture always occur together.

4.2. Evolution of RA and AF Values

In this section, only the data collected by one channel were analyzed to avoid the overlapping of signals collected by different channels. The data collected by sensor-1 were selected to analyze, and the moving average of these parameters was calculated from 50 AE events.

The evolution law of the RA and AF values of red sandstone in the three test types with time is shown in Figure 8. The RA and AF values show ups and downs before T_t; however, they show obvious trends after T_t. When the loading time is in the interval between T_t and the final failure time (T_f), there is an obvious downward trend in RA value and an obvious upward trend in AF value. In addition, when rock failure occurs, the RA value will suddenly decrease, and the AF value will suddenly increase in the three test types.

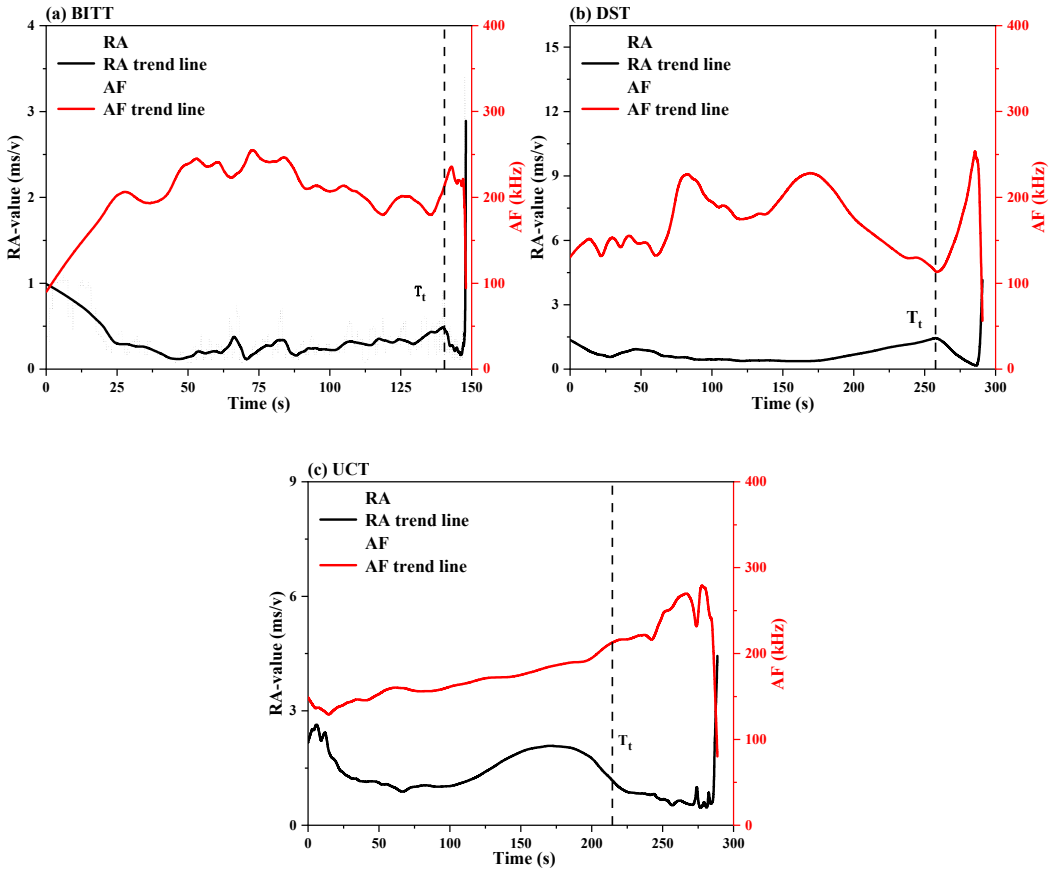

Figure 8. Temporal change of RA and AF values in different test types. (**a**) BITT; (**b**) DST; (**c**) UCT.

4.3. The Kernel Density Distribution of RA–AF Values

The RA–AF distribution can qualitatively describe the variation trend of shear and tensile fracture in the tested specimens. The density maps of RA–AF data in the three types of tests are shown in Figures 9–11, in which the density of data is lower in the red region and higher in the purple and blue regions. A change in color from red to purple indicates that the data distribution has changed from sparse to dense. With the color changing from red to purple, the distribution of data changes from sparse to dense. The purple and blue areas are called the main data distribution areas, which are marked with the black dot–dash square frame. Furthermore, a manual straight line of 45, passing through two points (0, 0) and (30, 1100) with a slope of 36.67, is drawn as the reference line to distinguish the RA–AF distribution. It can be seen from Section 4.2 that RA and AF

values vary greatly in different time periods. Therefore, T_t is selected as the dividing point to divide the loading process of each test into two phases, in which the RA–AF distribution is compared. Here, t represents the actual time, and T_f represents the moment when the sample failure occurs.

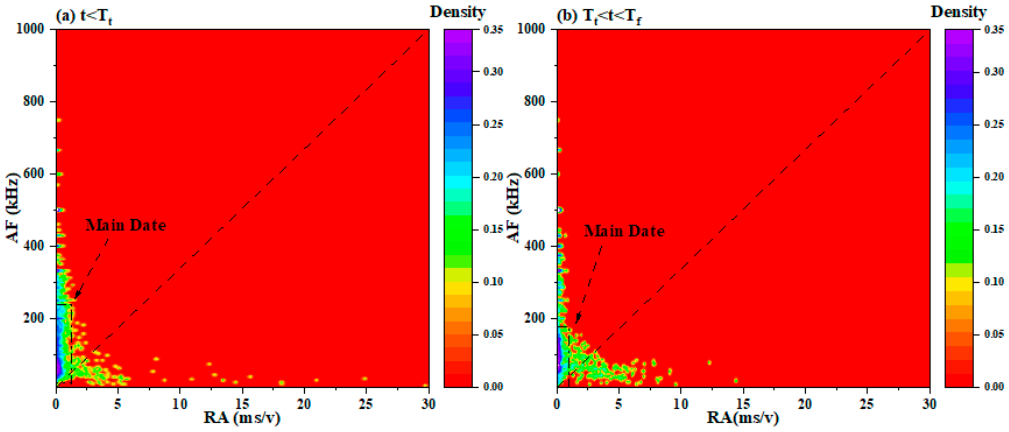

Figure 9. RA–AF data density maps in BITT. (**a**) $t < T_t$; (**b**) $T_t < t < T_f$.

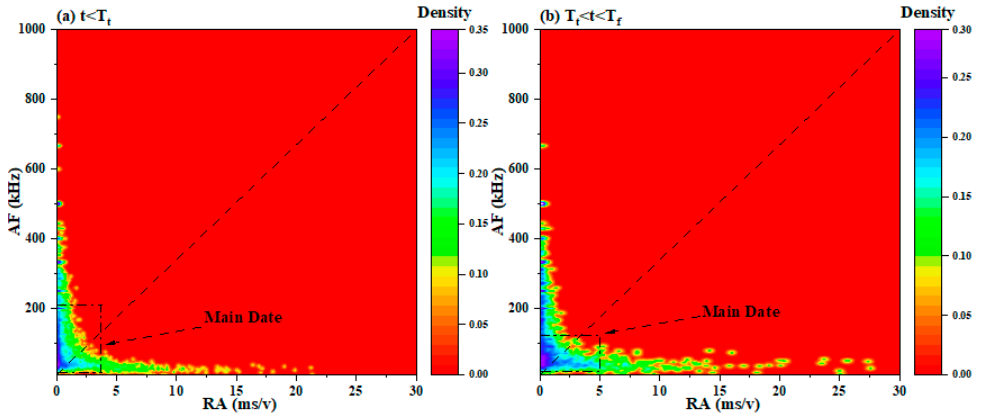

Figure 10. RA–AF data density maps in DST. (**a**) $t < T_t$; (**b**) $T_t < t < T_f$.

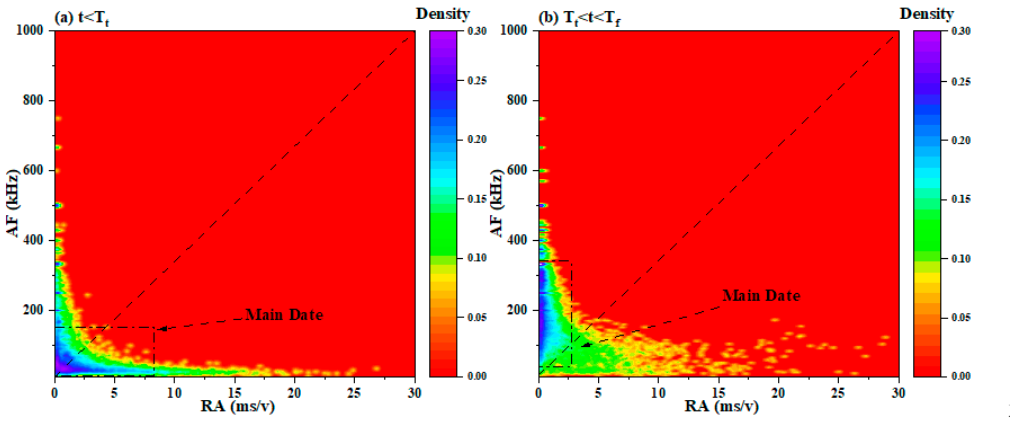

Figure 11. RA–AF data density maps in UCT. (**a**) $t < T_t$; (**b**) $T_t < t < T_f$.

Figure 9 shows that the data are mainly distributed above the reference line in BITT, and the RA–AF distribution in phase-1 and phase-2 is similar. From the main data, we can see that the main distribution range of AF values is 0–240 KHz, while the distribution of

RA values is in a smaller range (0–1 ms/v). Only a small amount of data is distributed below the reference line, indicating that the shear characteristic signal is dominant in BITT. Figure 10 shows that the main data above the reference line are still dominant in DST, while the main data below the reference line also increases significantly. There are differences in RA–AF distribution between phase-1 and phase-2. From the main data, we can see that the range in AF values in the two phases is 0–150 kHz, and the range in RA value in phase-1 is 0–3 ms/V, while the range in RA values in phase-2 is significantly increased, to 0–5 ms/V. This suggests that the shear characteristic signals increase clearly with the increase in loading in DST. Figure 11 shows that the distribution of RA–AF data in the two phases of UCT is different. In phase-1, the main data are evenly distributed on the upper and lower sides of the reference line, and their distribution range is the rectangular area bounded by the RA value range of 0–8 ms/V and the AF value range of 0–180 kHz. In phase-2, the data are mainly distributed above the reference line. The range of AF values is 0–2.5 ms/V, and the range of RA values is 30–340 kHz. This suggests that shear and tensile characteristic signals are generated simultaneously in the microcrack generation phase in UCT, while tensile characteristic signals are mainly generated in the macrocrack generation phase.

4.4. Classification of Tensile and Shear Cracks

It can be seen from Section 4.3 that the RA–AF distribution in BITT and DST mainly presents obvious tensile characteristic signals and shear characteristic signals, respectively. Therefore, the RA–AF data in BITT and DST were selected for analysis to determine the dividing line of RA–AF distribution between tensile and shear cracks in red sandstone samples. The method used to determine the dividing line as to plot the RA–AF data in BITT and DST on the same scatter diagram, and then find a straight line so that the data proportion under the straight line in BITT is basically the same as that on the straight line in DST [26]. An enlargement of the main data in Figures 10b and 11b is shown in Figure 12, in which it can be seen that the straight line (AF = 75 kHz) is a reference line. There are obvious differences between the RA–AF distributions above and below the reference line, regardless of whether we are using BITT or DST. Hence, the value of 75 kHz has been selected as the intercept of the dividing line. Next, the dividing line was determined by constantly changing the slope. When the slope of the dividing line reached the value of 93, both the data proportion in BITT below the line and that in DST above the line were 39.9%. Therefore, the straight line, AF = 93RA + 75, was determined as the dividing line between the tensile crack and shear crack in the RA–AF scatter plots, as shown in Figure 13.

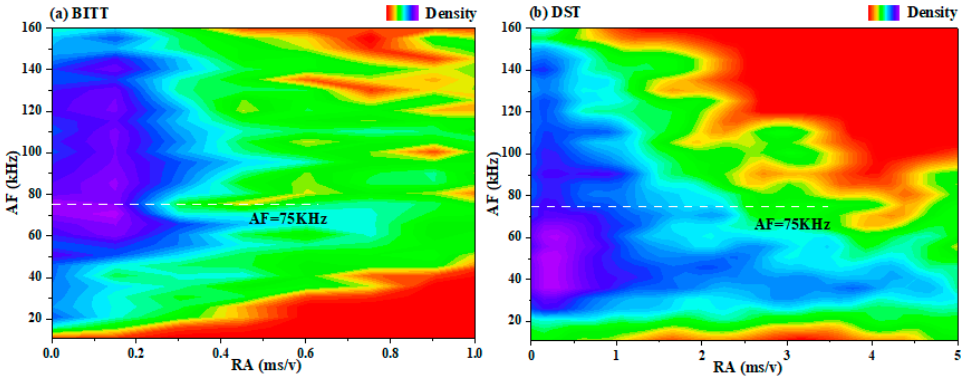

Figure 12. Enlarged figure of the main data in BITT and DST. (**a**) BITT; (**b**) DST.

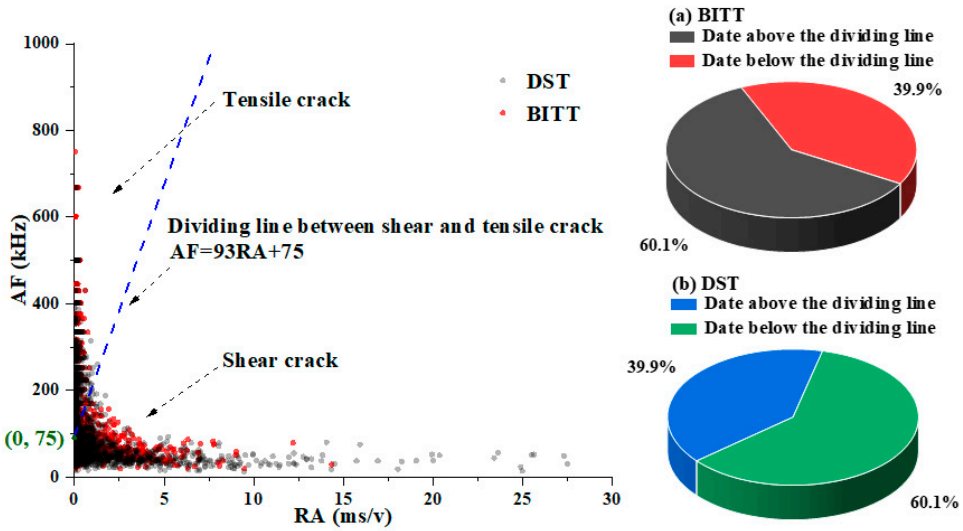

Figure 13. Determinations of the dividing line between tensile and shear cracks. (**a**) BITT; (**b**) DST.

As shown in Figure 13, we have determined that the dividing line between tensile fracture and shear fracture in the RA–AF scatter plots of red sandstone is AF = 93RA + 75. The RA–AF data distributed above the dividing line represent the data generated by tensile fracture, and the RA–AF data distributed below the dividing line represent the data generated by shear fracture. Therefore, the AE monitoring technology can classify between tensile fracture and shear fracture in the whole process of rock loading. When a fracture occurs, the RA–AF value of the collected AE signal is distributed above the dividing line (AF > 93RA + 75), which can be considered as a tensile fracture. On the contrary, if the RA–AF value is distributed below the division line (AF < 93RA + 75), the fracture can be considered as a shear fracture.

4.5. Statistics of Tension and Shear Fracture, and Analysis of Failure Mechanism

According to the dividing line determined above, the microcracks of red sandstone under uniaxial compression test loading are statistically analyzed. The statistics of the tensile and shear cracks of the U-1, U-2 and U-3 specimens are shown in Figure 14. The total numbers of AE events in the U-1, U-2 and U-3 specimens are 38,783, 51,200 and 45,264, respectively. It can be seen in Figure 14 that tensile cracks account for a large proportion (more than 67%) in the U-1 specimen, while shear cracks account for a large proportion (about 60%) in the U-2 and U-3 specimens, which indicates that the fracture mode of rock under uniaxial compression loading is complex. In addition, by observing the failure modes of the U-1, U-2 and U-3 specimens (Figure 15), it can be found that the U-1 specimen with more tensile cracks is broken, while the U-2 and U-3 specimens with more shear cracks are more complete. The macroscopic cracks on the surface of each specimen are mainly shear cracks, accompanied by a certain number of tensile cracks. These results correspond to the results reflected by AE parameters, but they still need to be further analyzed from the perspective of the rock failure mechanism.

Griffith crack exists in rock material at the initial state. Griffith cracks in rocks can be formed by pores, voids, soft or hard nodules or particles, particle boundaries, etc. [64–66]. When the shear stress on the fracture surface exceeds the shear strength, shear fracture will occur in the rock, which is the main fracture mode.

When the extension direction of the crack in the rock is approximately parallel to the direction of the compressive stress, the tensile stress will concentrate at the tip of the crack under the compressive stress [67]. If the tensile stress concentration is large and reaches the tensile strength of the material, the crack will begin to expand. In this case, the pressure

will continue to increase, and the crack will expand rapidly, which may eventually lead to a macrofracture.

If the crack extension direction in the rock intersects with the compressive stress direction at a small angle, we take out an "isolator" containing an inclined crack AB from the rock sample along the axis, as shown in Figure 16. With the gradual increase in axial pressure, shear slip will occur along the crack's surface in the rock specimen. In the above case, normal stress N and friction force F occur on the shear slip surface, and the combined stress along the axial direction is less than the axial stress in the rock specimen; otherwise there will be no slip (shear) fracture. Therefore, there must be shear stress on the BG surface to balance the axial stress. In addition, the shear slip action will also produce a tensile stress perpendicular to the axial direction, which increases with the increase in the slip surface. Obviously, in the compression process, without confining pressure or with very small confining pressure, a tensile fracture along the axial direction will occur with the increase in the shear slip surface. After a tensile fracture surface appears, the axial shear and the tensile stress of the rock specimens below it (along the slip surface) will be reduced to zero. Then, with the continuous expansion of the shear surface, tensile fractures will occur one by one [68,69]. Therefore, when there are many Griffith cracks in the rock that are approximately parallel to the direction of the compressive stress, or within a small angle, shear fracture and tensile fracture occur simultaneously in the rock.

Obviously, the above rock failure mechanism corresponds to the rock failure characteristics reflected by the AE parameters. Therefore, the proposed dividing line of RA–AF scatter plots can be used for classifying tensile and shear fractures to determine the fracture mode of red sandstone.

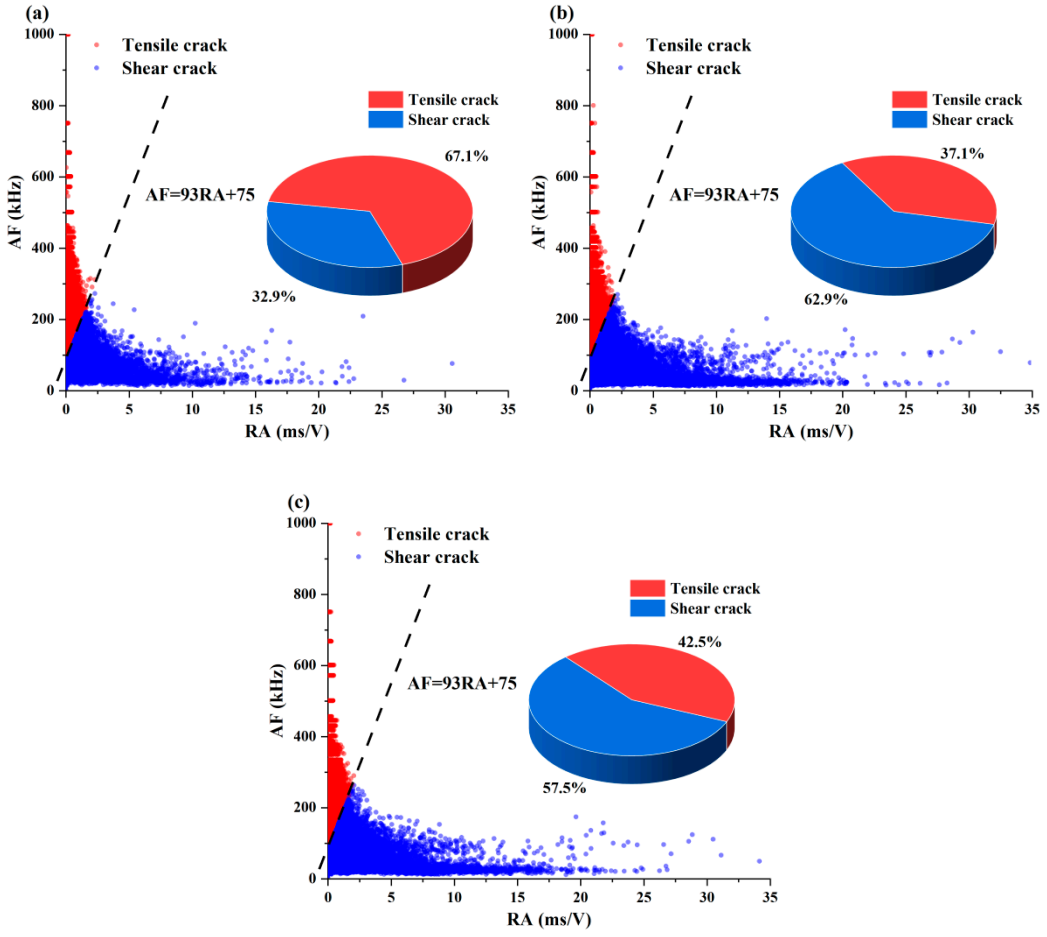

Figure 14. The statistics of tensile and shear cracks of the U-1, U-2 and U-3 specimens. (**a**) BITT; (**b**) DST; (**c**) UCT.

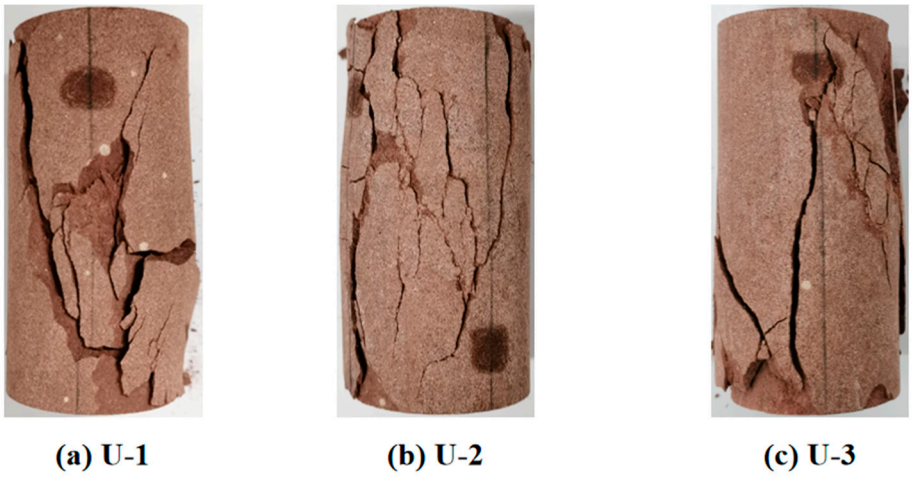

Figure 15. The failure modes of the U-1, U-2 and U-3 specimens. (**a**) BITT; (**b**) DST; (**c**) UCT.

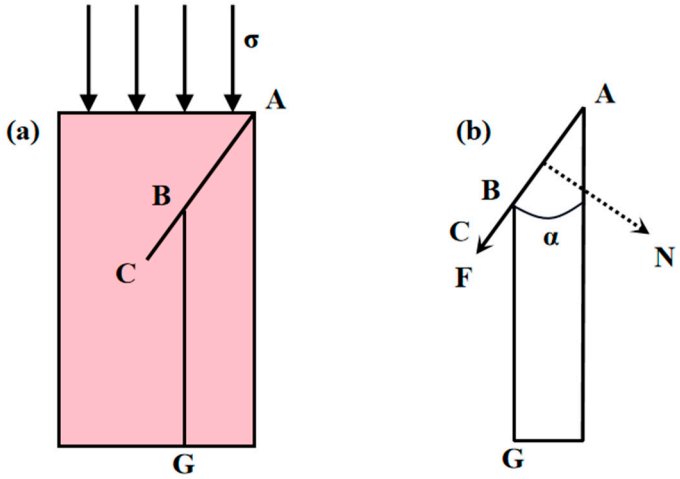

Figure 16. Shear and tensile failure mechanism of rock specimen. (**a**) Isolator; (**b**) stress diagram.

5. Discussion

Having determined the dividing line (AF = 93RA + 75) between shear and tensile cracks, we focus on the evolution law of tension and the shear sources of sandstone in UCT on the basis of RA and AF values. In addition, combined with the statistical index analysis of the b-value, the failure precursor index of red sandstone is here discussed based on the dividing line. In this section, the analysis is based on the data of U-1, U-2 and U-3 specimens.

5.1. Evolution Characteristics of Tensile and Shear Sources in UCT

When the signal generated by a fracture is received by multiple sensors (greater than or equal to four) at the same time, a positioning signal, the fracture source, will be formed. Because it is difficult for a fracture signal to be collected by multiple sensors at the same time, the location source data in this section are much fewer than the number of acoustic emission events in the above section.

The two-dimensional spatial distribution of tensile and shear AE sources in each sample is shown in Figure 17, in which the distribution of the AE source of red sandstone is relatively scattered under the condition of uniaxial compression, which is generally consistent with the position of the macro failure surface of the specimen. The total numbers

of sources of U-1, U-2, and U-3 specimens are 1062, 1001, and 1388, respectively, most of which are tensile sources. The percentages of tensile sources of the U-1, U-2, and U-3 specimens in the total number of sources are 84.7%, 77.4%, and 71.4%, respectively, as shown in Figure 18. Compared with Figure 14, it is found that although shear cracks account for a large proportion of microcracks in U-2 and U-3, the fracture sources are mainly tensile sources, indicating that tensile fracture more easily forms a positioning signal.

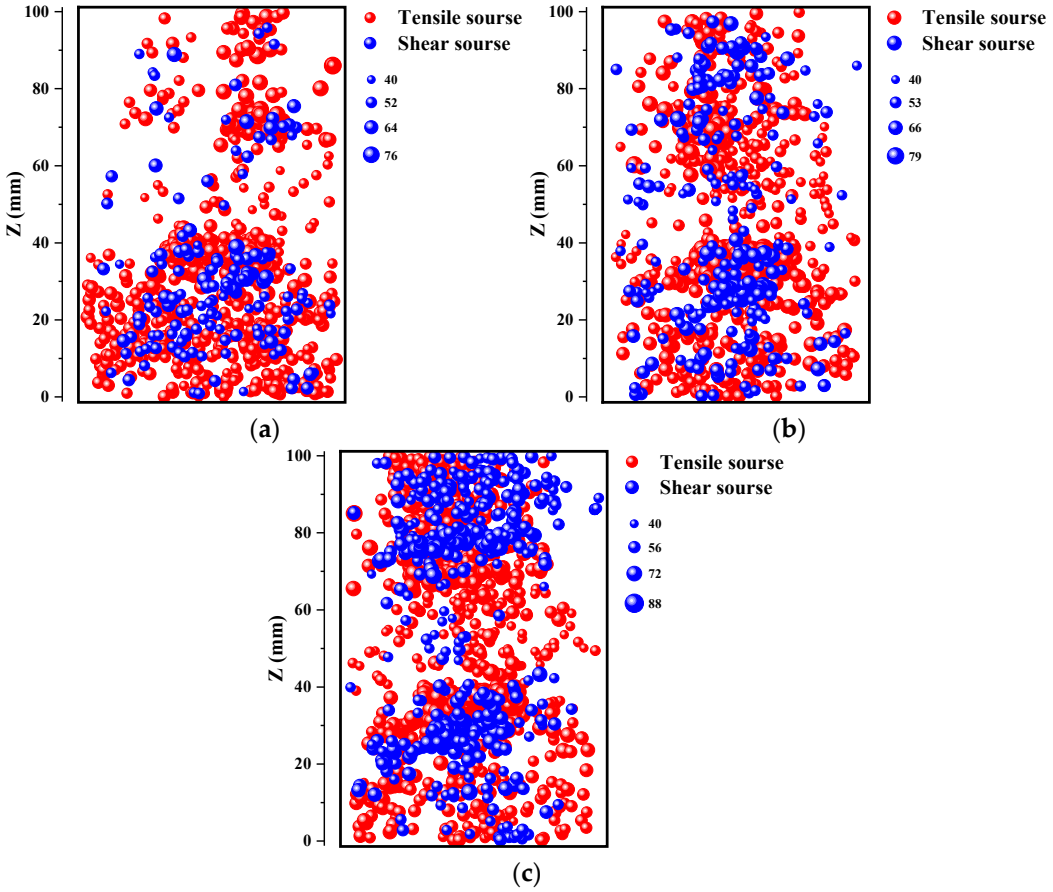

Figure 17. Spatial distribution of AE sources: (**a**) U-1; (**b**) U-2; (**c**) U-3. **Note:** The size of the scatter diagram indicates the source amplitude.

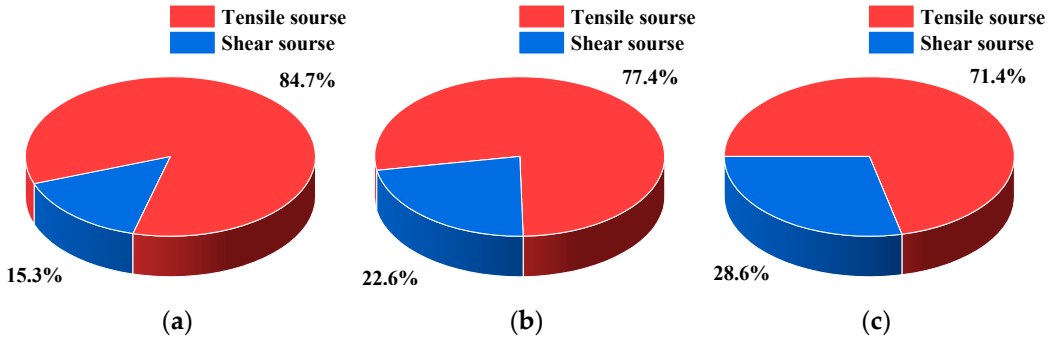

Figure 18. Percentage of different types of AE sources: (**a**) U-1; (**b**) U-2; (**c**) U-3.

Figure 19 shows the cumulative number of tensile and shear AE sources corresponding to axial strain throughout the whole process for three specimens, including the total stress–strain curve. According to the deformation characteristics of specimens, the approximate straight line section of the stress–strain curve can be defined as the phase from the elastic deformation to the stable development of microcracks (II), and the phase before

elastic deformation to the stable development of microcracks (II) can be defined as the micropore compaction phase (I). In addition, after the elastic deformation reaches the stable development phase of microcracks (II), before peak stress occurs, the unstable development phase of microcracks emerges (III). The slopes of the approximate straight lines of the stress–strain curves for the U-1, U-2, and U-3 specimens are 210.89, 188.31, and 214.78, respectively.

A fascinating phenomenon was found, whereby shear sources always grow prior to tensile sources in the initial phase I. This phenomenon depends on the initial micro pore and microcrack state of each specimen, to a certain extent. With the increase in loading stress, there is a rapid growth point in the number of tensile sources. The stress corresponding to the rapid growth point of the tensile source of the U-1, U-2, and U-3 specimens is 83.09%σ_t, 57.22%σ_t and 70.25%σ_t, respectively (σ_t is the peak stress). The rapid growth point of the tensile source of the U-1 specimen is at the critical point of phase II and phase III, and the rapid growth points of the tensile sources of the U-2 and U-3 samples are all at phase II. However, in phase I, the shear source increases rapidly; in phase II, the growth of the shear source is slow, and its cumulative curve is roughly "horizontal". The rapid growth point of the shear source appears in phase III, which is close to rock failure. The stress corresponding to the rapid growth points of the shear sources of the U-1, U-2, and U-3 specimens is 99.49%σ_t, 95.46%σt, and 95.93%σ_t, respectively. Owing to the strength of the U-2 specimen being lower than that of the U-1 and U-3 specimens, the rapid growth point of the U-2 specimen occurs earlier, and especially the rapid growth point of the tensile source.

It can be seen from the above analysis that under uniaxial compression loading, the fracture source of red sandstone is primarily the shear source in the initial phase of loading and the tensile source in the critical failure phase, and the number is far greater than that of the shear source.

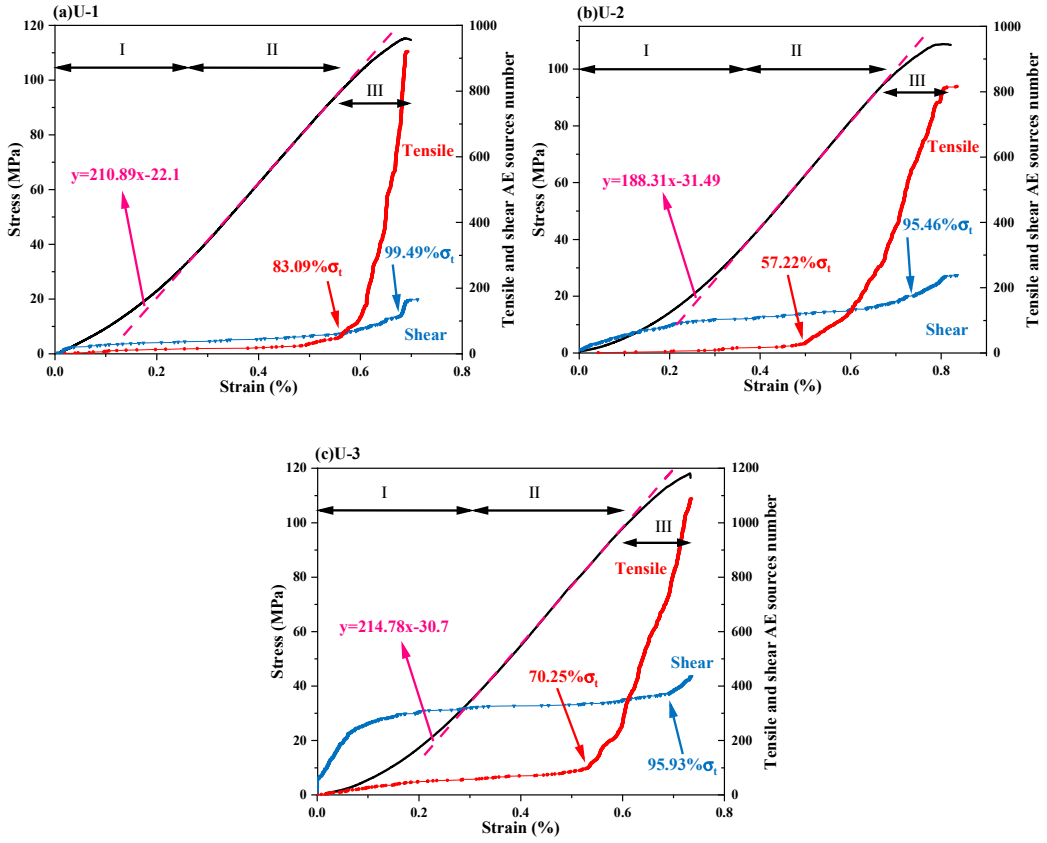

Figure 19. Curves of AE source numbers with axial strain: (**a**) U-1; (**b**) U-2; (**c**) U-3.

5.2. Failure Precursor Index of Rock Based on k Value

There will be certain contingencies in the parameters obtained in AE monitoring. The instantaneous growth of a certain index may be unable to objectively reflect the intensification of fracture in the rock. Therefore, in the AE monitoring based on parameter analysis, the AE parameters are usually statistically processed to further obtain the corresponding statistical indicators.

Among the statistical indicators based on amplitude, the most commonly used is the b-value statistic. The b-value originates from the Gutenberg Richter (G-R) relationship in seismology; that is, the logarithm of cumulative times (N), greater than magnitude (M), is linear with magnitude (M) [70], as shown in Formula (13).

$$\log N = a - bM \tag{13}$$

where a and b are constants. In the analysis of AE parameters, the amplitude can usually be divided by 20 to represent the AE magnitude M, i.e., M = A/20. In the calculation of the b-value, the unit of A is dB.

The B-value is mainly used to measure the relative number of small-magnitude fracture events and large-magnitude fracture events in rocks under compression, which can represent the scale of magnitude distribution of AE events. Therefore, it is widely used to analyze and forecast the precursors of rock fracture [71]. When the b-value is larger, it indicates that small- and medium-scale fracture events account for a large proportion; otherwise, it indicates that large-scale fracture events are dominant. In laboratory test, the corresponding b-value is about 1 (±0.5), when the rock mass fails.

In addition, in previous studies, the dividing line between shear and tensile crack was in the form of y = kx. In the analysis of the fracture mechanism, the slope of the dividing line, k = AF/RA, was used as an index to classify the shear fracture and tensile fracture. However, the intercept of the dividing line proposed in this paper is not zero, so the k-value, k = AF/(93RA + 75), is selected as the AE parameter index to estimate the damage degree of the red sandstone specimens. When the number of signals with large k-value increases, it indicates that the proportion of tensile fracture in the specimen increases, and the damage intensifies. For k-value, the instantaneous accidental value is also not enough to explain the intensification of fracture. Therefore, it is difficult to estimate the severity of specimen failure when only using the absolute k-value of one or several AE signals. In this study, the coefficient of variation (CV) is selected as the statistical index, and the dispersion of k-value distribution is used to describe the fracture of specimens. As a normalized measure indicator, CV is defined as the ratio of the standard deviation to the average.

Figure 20 shows the statistical results of the b-value and the CV (k) of the U-1, U-2, and U-3 specimens, taking the strain as the independent variable. In the process of calculation, the AE data of each specimen were equally divided into 100 segments, and then the corresponding b-value and CV (k) of each segment were calculated. The sample sizes of the U-1, U-2, and U-3 specimens are 240, 199, and 269 respectively. In Figure 14, the phase partition from Figure 13 is used again. Since the data in the pink dotted rectangle in the figure are too dense, the data in this area are enlarged. Furthermore, two kinds of reference lines are set in the figure. One is a horizontal dotted line, which corresponds to b-value = 1 and CV (k) = 1; the other is the vertical dotted line, which corresponds to the rapid growth point of the tensile source, as described in Section 5.1.

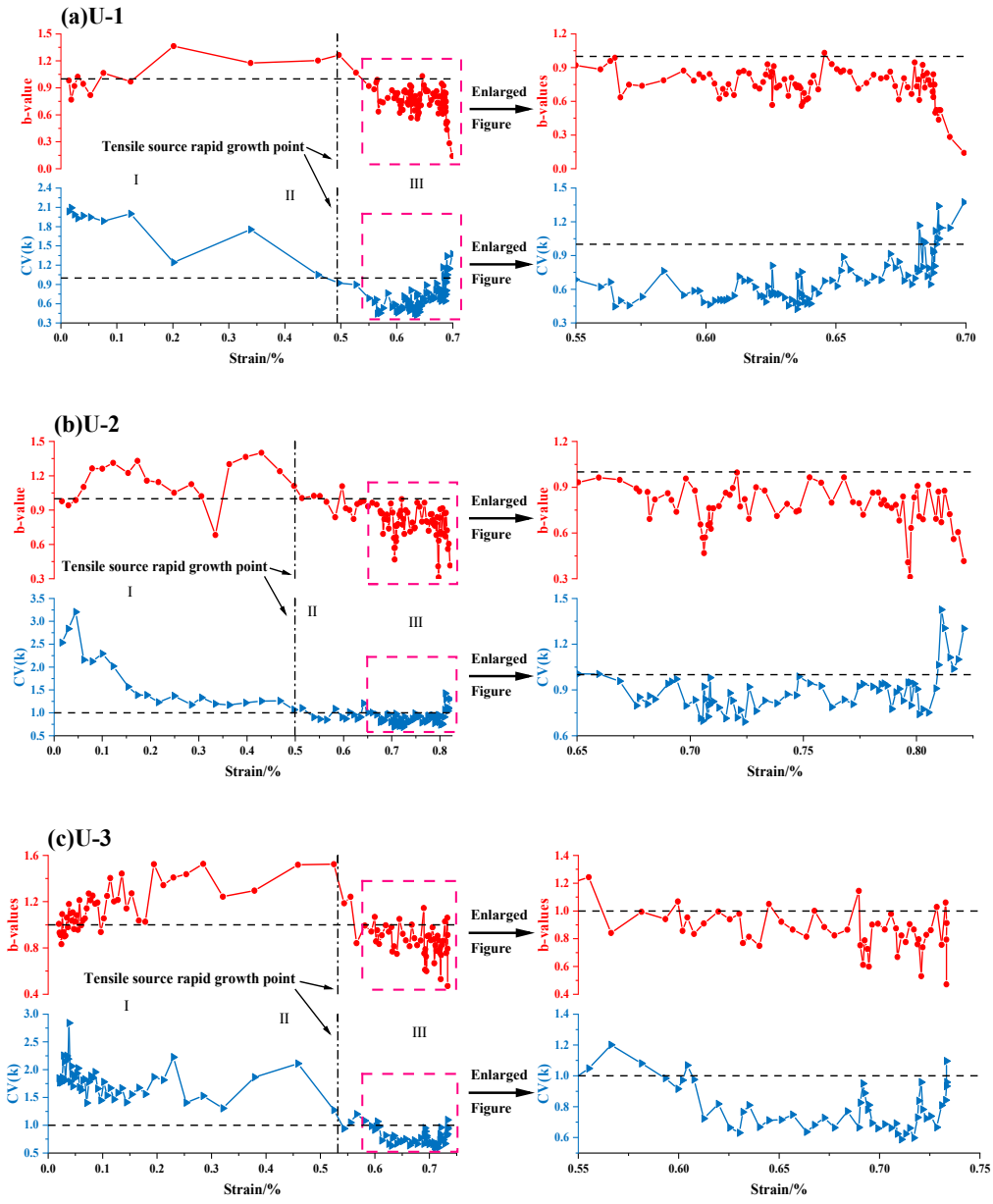

Figure 20. Comparison of CV(r) and b-values among different specimens. (**a**) U-1; (**b**) U-2; (**c**) U-3.

It can be seen from Figure 20 that when the strain of all specimens reaches the corresponding rapid growth point of the tensile source, the b-values decrease significantly, and when the b-values decrease to less than 1, the specimen will enter phase-III. In phase-III, except for individual points, the other b-values are less than 1, and when the specimen is close to complete failure, the b-values decrease significantly again. Additionally, when the strain of all specimens approaches the rapid growth point of the corresponding tensile source, CV (k) shows a downward trend, and the first CV (k) behind the vertical reference line is close to 1. In phase-III, the CV (k) of all specimens is stable at less than 1. Differently from the b-value, when the specimen is close to complete failure, the CV (k) increases significantly and will exceed 1.

In the early loading phase of all specimens, the b-values were basically distributed between 0.7 and 1, and then increased to 1–1.5, which indicates that the micropores of the specimens were gradually compacted at the initial phase of loading, and then small fractures dominated in the specimens. However, until the specimens approached the failure phase and were in the failure phase, the b-value began to decrease sharply. The b-value

of the U-2 specimen suddenly decreased in the early phase of loading, but then returned to a higher level, which indicates that some large-scale fractures appeared in this phase, but did not continue to develop, and returned to the fracture development mode dominated by small-scale fractures.

In the early loading phase of all specimens, the span of CV (k), basically distributed between 1 and 3.4, was large, which means that the dispersion of the k-value was large, indicating that there were great differences, with tensile cracks and shear cracks occurring together, in the crack types of the specimens in the early loading phase. However, when the strain reached the corresponding rapid growth point of the tensile source, especially after the specimen entered phase-III, the CV (k) was relatively stable, which means that the dispersion of the k-value was small, indicating that tensile cracks were mainly produced. Meanwhile, in phase-III, the CV (k) also increased locally on the basis of relative stability, especially when the specimens were close to complete failure, which increased significantly. This shows that a small number of shear cracks were also generated in the specimen in phase-III, and when the specimen was in complete failure, a large number of shear cracks were generated.

From the above results, it can be found that the combination of b-value and CV (k) can reveal the failure process of a specimen. In the early (stable) failure phase, the b-value was mainly distributed between 1 and 1.5, while the CV (k) value's distribution span was large, ranging from 1 to 3.4; in the instability failure phase, both the b-value and CV (k) were less stable than 1. Only when the final failure occurred did CV (k) increase significantly, and come to exceed 1. Therefore, 1.0 can also be used as the recommended judgment value of the CV (k) index.

In a practical sense, when the CV (k) is greater than 1, the dispersion of the k-value exceeds 100%. It can be seen from the above conclusions that in the unstable failure phase, tensile fracture is the main fracture type, and the corresponding k-values are large. With the aggravation of the fracture, when the specimen is in complete failure, the proportion of shear fracture signal increases, and more signals with small k-value appear.

The dispersion of k-values exceeding 100% indicates that the number of AE signals with small k-value increased significantly, and the proportion of shear fracture signals increased significantly. Therefore, taking CV (k) as the fracture failure judgment value of red sandstone has practical significance.

6. Conclusions

The AE characteristics of red sandstone in BITT, DST, and UCT were analyzed using AE monitoring technology. The variation law of the RA and AF values was analyzed to study the fracture mode and propagation characteristics of cracks in red sandstone. Based on the kernel density estimation (KDE) function and coupling the AE parameters (RA–AF values) in DST and BITT, the classification method of red sandstone fractures was determined. The reliability of this method was verified by the results of uniaxial compression tests. The conclusions are as follows:

(1) AE event rate can reflect the transformation of rock samples from microcracks to macrocracks. The macrocrack generation phase in UCT was the longest, that in DST was the second longest, and that in BITT was the shortest;
(2) The KDE method can effectively identify and visualize the high-density areas of RA and AF values. In the failure mode dominated by tensile fracture, the RA value was low and the AF value was high. On the contrary, in the failure mode dominated by shear fracture, the RA value was high and the AF value was low. When rock failure occurred, the RA and AF values both developed in opposite directions;
(3) It was determined that the dividing line for classifying tensile and shear cracks in the RA and AF value data is AF = 93RA + 75. The reliability of the dividing line has been verified by analyzing the failure mode and fracture mechanism of the sample;

(4) Under uniaxial compression loading, the fracture source of red sandstone was mainly the shear source in the initial phase of loading, and the tensile source in the critical failure phase, and the number of the latter was far greater than that of the shear source;
(5) K = AF/(93RA + 75) was proposed as an AE parameter index to reflect the internal fracture of the red sandstone specimen. Further, the corresponding reference judgment value CV (k) = 1 was proposed. It can be considered that the test sample entered the instability failure phase when CV (k) < 1.

Author Contributions: Conceptualization, J.L. and C.W.; data curation, J.L.; formal analysis, Y.H.; funding acquisition, C.W. and S.L.; investigation, J.L.; methodology, C.W.; project administration, Y.H.; resources, C.W.; software, S.L.; supervision, C.W. and S.L.; validation, S.L. and C.W.; visualization, Y.H.; writing (original draft), J.L.; writing (review and editing), J.L. and S.L. All authors have read and agreed to the published version of the manuscript.

Funding: This research was funded by National Natural Science Foundation of China (No. 52004072, No. 52064006, and No. 52164001), the Guizhou Provincial Science and Technology Foundation (No. [2020]4Y044, No. [2021]292, [2021]4023, and [2021]N404), and the Guizhou Provincial Graduate Research Foundation (YJSCXJH[2020]088).

Institutional Review Board Statement: Not applicable.

Informed Consent Statement: Informed consent was obtained from all subjects involved in the study.

Data Availability Statement: Some or all data, models, or codes that support the findings of this study are available from the corresponding author (fgan@gzu.edu.cn.) upon reasonable request.

Conflicts of Interest: The authors declare no conflict of interest.

Abbreviations

AE	Acoustic emission
BITT	Brazilian indirect tensile test
DST	Direct shear test
UCT	Uniaxial compression test
KDE	Kernel density estimation
RA	RA = rise time/amplitude
AF	Average frequency
σ_s	Shear strength
σ_c	Uniaxial compressive strength
$F(\tau)$	The inter-event time function/AE event rate
T_t	Time at the beginning of drastic increase in AE events
F_t	Load at the beginning of drastic increase in AE events
F_p	Peak load during the test
CV	The coefficient of variation

References

1. Bi, J.; Zhou, X.P.; Qian, Q.H. The 3D numerical simulation for the propagation process of multiple pre-existing flaws in Rock-Like materials subjected to biaxial compressive loads. *Rock Mech. Rock Eng.* **2016**, *49*, 1611–1627.
2. Zhao, Y.; Zhang, C.; Wang, Y.; Lin, H. Shear-related roughness classification and strength model of natural rock joint based on fuzzy comprehensive evaluation. *Int. J. Rock Mech. Min.* **2021**, *137*, 104550.
3. Zhao, Y.; Zhang, Y.; Yang, H.; Liu, Q.; Tian, G. Experimental study on relationship between fracture propagation and pumping parameters under constant pressure injection conditions. *Fuel* **2022**, *307*, 121789.
4. Tang, L.; Zhao, Y.; Liao, J.; Liu, Q. Creep experimental study of rocks containing weak interlayer under multilevel loading and unloading cycles. *Front. Earth Sci.* **2020**, *480*, 519461.
5. Zhao, Y.; He, P.; Zhang, Y.; Wang, C. A new criterion for a Toughness-Dominated hydraulic fracture crossing a natural frictional interface. *Rock Mech. Rock Eng.* **2019**, *52*, 2617–2629.

6. Zhao, Y.; Bi, J.; Wang, C.; Liu, P. Effect of unloading rate on the mechanical behavior and fracture characteristics of sandstones under complex triaxial stress conditions. *Rock Mech. Rock Eng.* **2021**, *54*, 4851–4866.
7. Zhao, Y.; Liu, Q.; Zhang, C.; Liao, J.; Lin, H.; Wang, Y. Coupled seepage-damage effect in fractured rock masses: Model development and a case study. *Int. J. Rock Mech. Min.* **2021**, *144*, 104822.
8. Zhao, Y.; Wang, Y.; Wang, W.; Tang, L.; Liu, Q.; Cheng, G. Modeling of rheological fracture behavior of rock cracks subjected to hydraulic pressure and far field stresses. *Theor. Appl. Fract. Mech.* **2019**, *101*, 59–66.
9. Zhao, Y.; Zhang, L.; Liao, J.; Wang, W.; Liu, Q.; Tang, L. Experimental study of fracture toughness and subcritical crack growth of three rocks under different environments. *Int. J. Geomech.* **2020**, *20*, 04020128.
10. Zhao, Y.; Wang, C.L.; Bi, J. Analysis of fractured rock permeability evolution under unloading conditions by the model of elastoplastic contact between rough surfaces. *Rock Mech. Rock Eng.* **2020**, *53*, 5795–5808.
11. Zhang, S.; Wu, S.; Chu, C.; Guo, P.; Zhang, G. Acoustic emission associated with Self-Sustaining failure in Low-Porosity sandstone under uniaxial compression. *Rock Mech. Rock Eng.* **2019**, *52*, 2067–2085.
12. Liang, Z.; Xue, R.; Xu, N.; Li, W. Characterizing rockbursts and analysis on frequency-spectrum evolutionary law of rockburst precursor based on microseismic monitoring. *Tunn. Undergr. Space Tech.* **2020**, *105*, 103564.
13. Aggelis, D.G. Classification of cracking mode in concrete by acoustic emission parameters. *Mech. Res. Commun.* **2011**, *38*, 153–157.
14. Aggelis, D.G.; Mpalaskas, A.C.; Matikas, T.E. Acoustic signature of different fracture modes in marble and cementitious materials under flexural load. *Mech. Res. Commun.* **2013**, *47*, 39–43.
15. Zhao, Y.; Ding, D.; Bi, J.; Wang, C.; Liu, P. Experimental study on mechanical properties of precast cracked concrete under different cooling methods. *Constr. Build. Mater.* **2021**, *301*, 124141.
16. Zhang, J.; Zhou, X. AE event rate characteristics of flawed granite: From damage stress to ultimate failure. *Geophys. J. Int.* **2020**, *222*, 795–814.
17. Jiang, R.; Dai, F.; Liu, Y.; Li, A.; Feng, P. Frequency characteristics of acoustic emissions induced by crack propagation in rock tensile fracture. *Rock Mech. Rock Eng.* **2021**, *54*, 2053–2065.
18. Zhou, X.; Zhang, J.; Qian, Q.; Niu, Y. Experimental investigation of progressive cracking processes in granite under uniaxial loading using digital imaging and AE techniques. *J. Struct. Geol.* **2019**, *126*, 129–145.
19. Fu, X.; Ban, Y.; Xie, Q.; Abdullah, R.A.; Duan, J. Time delay mechanism of the kaiser effect in sandstone under uniaxial compressive stress conditions. *Rock Mech. Rock Eng.* **2021**, *54*, 1091–1108.
20. Zhao, Y.; Zheng, K.; Wang, C.; Bi, J.; Zhang, H. Investigation on model-I fracture toughness of sandstone with the structure of typical bedding inclination angles subjected to three-point bending. *Theor. Appl. Fract. Mec.* **2022**, *119*, 103327.
21. Yang, H.; Lin, H.; Chen, Y.; Wang, Y.; Zhao, Y.; Yong, W.; Gao, F. Influence of wing crack propagation on the failure process and strength of fractured specimens. *Bull. Eng. Geol. Environ.* **2022**, *81*, 71.
22. Liao, J.; Zhao, Y.; Tang, L.; Liu, Q.; Sarmadivaleh, M. Experimental Studies on Cracking and Local Strain Behaviors of Rock-Like Materials with a Single Hole before and after Reinforcement under Biaxial Compression. *Geofluids* **2021**, 8812006.
23. Zhao, Y.; Wang, Y.; Tang, L. The compressive-shear fracture strength of rock containing water based on Druker-Prager failure criterion. *Arab. J. Geosci.* **2019**, *12*, 452.
24. Lacidogna, G.; Piana, G.; Accornero, F.; Carpinteri, A. Multi-technique damage monitoring of concrete beams: Acoustic Emission, Digital Image Correlation, Dynamic Identification. *Constr. Build. Mater.* **2020**, *242*, 118114.
25. Zhang, Z.; Deng, J. A new method for determining the crack classification criterion in acoustic emission parameter analysis. *Int. J. Rock Mech. Min.* **2020**, *130*, 104323.
26. Du, K.; Li, X.; Tao, M.; Wang, S. Experimental study on acoustic emission (AE) characteristics and crack classification during rock fracture in several basic lab tests. *Int. J. Rock Mech. Min.* **2020**, *133*, 104411.
27. Zhao, Y.; Zhang, L.; Wang, W.; Tang, J.; Lin, H.; Wan, W. Transient pulse test and morphological analysis of single rock fractures. *Int. J. Rock Mech. Min.* **2017**, *91*, 139–154.
28. Zhao, Y.; Liu, Q.; Liao, J.; Wang, Y.; Tang, L. Theoretical and numerical models of rock wing crack subjected to hydraulic pressure and far-field stresses. *Arab. J. Geosci.* **2020**, *13*, 926.
29. Chai, M.; Hou, X.; Zhang, Z.; Duan, Q. Identification and prediction of fatigue crack growth under different stress ratios using acoustic emission data. *Int. J. Fatigue* **2022**, *160*, 106860.
30. Zhang, F.; Yang, Y.; Fennis, S.A.A.M.; Hendriks, M.A.N. Developing a new acoustic emission source classification criterion for concrete structures based on signal parameters. *Constr. Build. Mater.* **2022**, *318*, 126163.
31. Dong, L.; Tong, X.; Ma, J. Quantitative investigation of tomographic effects in abnormal regions of complex structures. *Engineering* **2021**, *7*, 1011–1022.
32. Gan, Y.; Wu, S.; Ren, Y.; Zhang, G. Evaluation indexes of granite splitting failure based on RA and AF of AE parameters. *Rock Soil Mech.* **2020**, *41*, 2324–2332.
33. Zhao, Y.; Zhang, L.; Wang, W.; Pu, C.; Wan, W.; Tang, J. Cracking and stress–strain behavior of Rock-Like material containing two flaws under uniaxial compression. *Rock Mech. Rock Eng.* **2016**, *49*, 2665–2687.
34. Tang, Y.; Lin, H.; Wang, Y.; Zhao, Y. Rock slope stability analysis considering the effect of locked section. *Bull. Eng. Geol. Environ.* **2021**, *80*, 7241–7251.
35. Ohno, K.; Ohtsu, M. Crack classification in concrete based on acoustic emission. *Constr. Build. Mater.* **2010**, *24*, 2339–2346.

36. JCMS-III B5706. *Monitoring Method for Active Cracks in Concrete by Acoustic Emission*; Federation of Construction Materials Industries: Tokyo, Japan, 2003.
37. Ohtsu, M. Rilem Technical Committee (Ohtsu M. Recommendation of RILEM TC 212-ACD: Acoustic emission and related NDE techniques for crack detection and damage evaluation in concrete. *Mater. Struct.* **2010**, *43*, 1187–1189.
38. 39.Zhao, Y.; Liao, J.; Wang, Y.; Liu, Q.; Lin, H.; Chang, L. Crack coalescence patterns and local strain behaviors near flaw tip for rock-like material containing two flaws subjected to biaxial compression. *Arab. J. Geosci.* **2020**, *13*, 1251.
39. Wang, H.; Liu, D.; Cui, Z.; Cheng, C.; Jian, Z. Investigation of the fracture modes of red sandstone using XFEM and acoustic emissions. *Theor. Appl. Fract. Mech.* **2016**, *85*, 283–293.
40. Lotidis, M.A.; Nomikos, P.P. Acoustic emission location analysis and microcracks' nature determination of uniaxially compressed calcitic marble hollow plates. *Geomech. Geophys. Geo-Energy Geo-Resour.* **2021**, *7*, 38.
41. Li, D.; Du, F. Monitoring and evaluating the failure behavior of ice structure using the acoustic emission technique. *Cold Reg. Sci. Technol.* **2016**, *129*, 51–59.
42. Han, Q.; Yang, G.; Xu, J.; Fu, Z.; Lacidogna, G.; Carpinteri, A. Acoustic emission data analyses based on crumb rubber concrete beam bending tests. *Eng. Fract. Mech.* **2019**, *210*, 189–202.
43. Triantis, D. Acoustic emission monitoring of marble specimens under uniaxial compression. Precursor phenomena in the near-failure phase. *Proced. Struct. Integr.* **2018**, *10*, 11–17.
44. Xie, Q.; Li, S.; Liu, X.; Gong, F.; Li, X. Effect of loading rate on fracture behaviors of shale under mode I loading. *J. Cent. South Univ.* **2020**, *27*, 3118–3132.
45. Wang, Y.; Peng, K.; Shang, X.; Li, L.; Liu, Z.; Wu, Y.; Long, K. Experimental and numerical simulation study of crack coalescence modes and microcrack propagation law of fissured sandstone under uniaxial compression. *Theor. Appl. Fract. Mech.* **2021**, *115*, 103060.
46. Liu, X.; Liu, Z.; Li, X.; Gong, F.; Du, K. Experimental study on the effect of strain rate on rock acoustic emission characteristics. *Int. J. Rock Mech. Min.* **2020**, *133*, 104420.
47. Zhang, H.; Wang, Z.; Song, Z.; Zhang, Y.; Wang, T.; Zhao, W. Acoustic emission characteristics of different brittle rocks and its application in brittleness evaluation. *Geomech. Geophys. Geo-Energy Geo-Resour.* **2021**, *7*, 48.
48. Meng, Y.; Jing, H.; Liu, X.; Yin, Q.; Wei, X. Experimental and numerical investigation on the effects of bedding plane properties on the mechanical and acoustic emission characteristics of sandy mudstone. *Eng. Fract. Mech.* **2021**, *245*, 107582.
49. Ge, Z.; Sun, Q. Acoustic emission characteristics of gabbro after microwave heating. *Int. J. Rock Mech. Min.* **2021**, *138*, 104616.
50. Chang, X.; Zhang, X.; Dang, F.; Zhang, B.; Chang, F. Failure behavior of sandstone specimens containing a single flaw under true triaxial compression. *Rock Mech. Rock Eng.* **2022**. https://doi.org/10.1007/s00603-021-02761-z.
51. Muñoz-Ibáñez, A.; Delgado-Martín, J.; Herbón-Penabad, M.; Alvarellos-Iglesias, J. Acoustic emission monitoring of mode I fracture toughness tests on sandstone rocks. *J. Petrol. Sci. Eng.* **2021**, *205*, 108906.
52. Li, L.R.; Deng, J.H.; Zheng, L.; Liu, J.F. Dominant frequency characteristics of acoustic emissions in white marble during direct tensile tests. *Rock Mech. Rock Eng.* **2017**, *50*, 1337–1346.
53. Niu, Y.; Zhou, X.; Berto, F. Evaluation of fracture mode classification in flawed red sandstone under uniaxial compression. *Theor. Appl. Fract. Mec.* **2020**, *107*, 102528.
54. Wang, Y.; Zhang, B.; Gao, S.H.; Li, C.H. Investigation on the effect of freeze-thaw on fracture mode classification in marble subjected to multi-level cyclic loads. *Theor. Appl. Fract. Mech.* **2021**, *111*, 102847.
55. Wang, Y.; Meng, H.; Long, D. Experimental investigation of fatigue crack propagation in interbedded marble under multilevel cyclic uniaxial compressive loads. *Fatigue Fract. Eng. Mater. Struct.* **2021**, *44*, 933–951.
56. Yao, Q.; Chen, T.; Tang, C.; Sedighi, M.; Wang, S.; Huang, Q. Influence of moisture on crack propagation in coal and its failure modes. *Eng. Geol.* **2019**, *258*, 105156.
57. Xiangqian, F.; Shengtao, L.; Xudong, C.; Saisai, L.; Yuzhu, G. Fracture behaviour analysis of the full-graded concrete based on digital image correlation and acoustic emission technique. *Fatigue Fract. Eng. Mater. Struct.* **2020**, *43*, 1274–1289.
58. Das, A.K.; Suthar, D.; Leung, C.K.Y. Machine learning based crack mode classification from unlabeled acoustic emission waveform features. *Cem. Concr. Res.* **2019**, *121*, 42–57.
59. Dong, L.; Chen, Y.; Sun, D.; Zhang, Y. Implications for rock instability precursors and principal stress direction from rock acoustic experiments. *Int. J. Min. Sci. Technol.* **2021**, *31*, 789–798.
60. Prem, P.R.; Murthy, A.R. Acoustic emission monitoring of reinforced concrete beams subjected to four-point-bending. *Appl. Acoust.* **2017**, *117*, 28–38.
61. Sagar, R.V.; Srivastava, J.; Singh, R.K. A probabilistic analysis of acoustic emission events and associated energy release during formation of shear and tensile cracks in cementitious materials under uniaxial compression. *J. Build. Eng.* **2018**, *20*, 647–662.
62. Triantis, D.; Kourkoulis, S.K. An alternative approach for representing the data provided by the acoustic emission technique. *Rock Mech. Rock Eng.* **2018**, *51*, 2433–2438.
63. Rippengill, S.; Worden, K.; Holford, K.M.; Pullin, R. Automatic classification of acoustic emission patterns. *Strain* **2003**, *39*, 31–41.
64. Wawersik, W.R. *Detailed Analysis of Rock Failure in Laboratory Compression Tests*; University of Minnesota: Minneapolis, MN, USA, 1968.
65. Hoek, E. Brittle fracture of rock. *Rock Mech. Eng. Pract.* **1968**, *130*, 9–124.
66. Jaeger, J.C. "*Brittle Fracture of Rocks." The 8th US Symposium on Rock Mechanics (USRMS)*; OnePetro: Richardson, TX, USA, 1966.

67. Li, M.; Qu, Y.; Qin, S.; Yan, X.; Sun, Q.; Ma, P. Criteria of swelling potential and analysis on failure mechanism for mud rock. *J. Eng. Geol.* **2009**, *17*, 633–637.
68. Chen, J.; Li, S.; Fracture failure mechanism of rock. *Adv. Earth Sci.* **2004**, *19*, 275–278.
69. Zhao, Y.; Wang, C.; Ning, L.; Zhao, H.; Bi, J. Pore and fracture development in coal under stress conditions based on nuclear magnetic resonance and fractal theory. *Fuel* **2022**, *309*, 122112.
70. Sagasta, F.; Zitto, M.E.; Piotrkowski, R.; Benavent-Climent, A.; Suarez, E.; Gallego, A. Acoustic emission energy b-value for local damage evaluation in reinforced concrete structures subjected to seismic loadings. *Mech. Syst. Signal Process.* **2018**, *102*, 262–277.
71. Guo, P.; Wu, S.; Zhang, G.; Chu, C. Effects of thermally-induced cracks on acoustic emission characteristics of granite under tensile conditions. *Int. J. Rock Mech. Min.* **2021**, *144*, 104820.